Volume 1
Number 5
1 September 2024
Pages 823–1095

RSC
Applied Interfaces

rsc.li/RSCApplInter

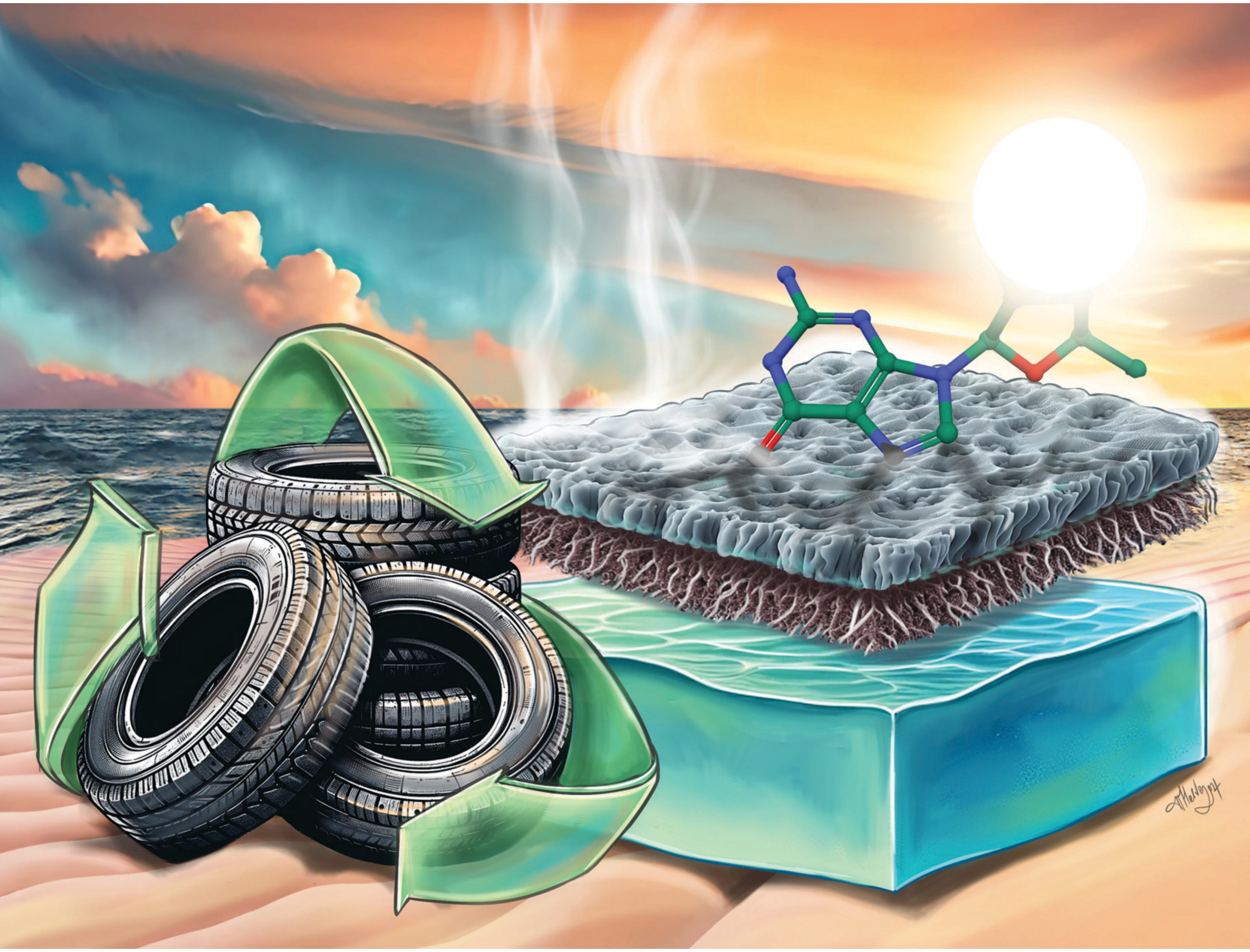

ISSN 2755-3701

ROYAL SOCIETY
OF **CHEMISTRY**

PAPER
Ali Koşar, Ali Sadaghiani *et al.*
Upcycled graphene nanoplatelets integrated fiber-based Janus membranes for enhanced solar-driven interfacial steam generation

RSC
Applied Interfaces

ROYAL SOCIETY
OF CHEMISTRY

PAPER

View Article Online
View Journal | View Issue

Check for updates

Cite this: *RSC Appl. Interfaces*, 2024, **1**, 896

Upcycled graphene nanoplatelets integrated fiber-based Janus membranes for enhanced solar-driven interfacial steam generation†

Jalal Karimzadeh Khoei,‡[ab] Mohammad Sajad Sorayani Bafqi,‡[abc] Kuray Dericiler,[ac] Omid Doustdar,[d] Burcu Saner Okan,[ac] Ali Koşar *[abe] and Ali Sadaghiani *[abe]

Received 9th March 2024,
Accepted 1st May 2024

DOI: 10.1039/d4lf00082j

rsc.li/RSCApplInter

The increasing demand for drinking water and environmental concerns related to fossil fuels have given rise to the use of solar energy in water desalination. Solar-driven interfacial steam generation is a promising method for water purification, particularly in remote areas. Janus membranes, featuring bilayer hydrophobic/hydrophilic structures, offer high functionality and have attracted significant interest in this field. This study explores the integration of novel graphene nanoplatelets (GNP) derived from waste tire pyrolysis through upcycling as a photothermal source in Janus membranes. The membranes consist of polyacrylonitrile (PAN) nanofibrous membranes for water supply and polymethyl methacrylate (PMMA)/graphene nanoplatelets (GNP) nanofibrous membranes for light harvesting. The effects of GNP content and layer thicknesses on photothermal activity, water transport, and overall evaporation rate were analyzed experimentally and numerically. The results showed that a decrease in membrane thickness led to a 19% to 63% enhancement in evaporation rate, highlighting the importance of optimizing membrane design for efficient water desalination.

Introduction

The increasing population and advancing economic development, coupled with changes in consumption patterns, drive a heightened demand for water. Over the past century, there has been a more than 600% increase in the worldwide demand for water.[1,2] Various methods have been utilized to produce freshwater, relying on traditional energy sources like fossil fuels. These include techniques such as membrane distillation (MD),[3] multi-stage flash (MSF) distillation,[4] and brine crystallizer (BCr),[5] all driven by fossil fuels. However, using fossil fuels has raised multiple concerns, including the depletion of natural resources,[6] global warming,[7] environmental pollutants,[8] and health,[9] and they come with higher operational costs and increased energy consumption. In contrast, solar energy has been extensively utilized across diverse applications as a viable replacement for fossil fuels. In water desalination systems, solar energy transforms into thermal energy *via* photothermal materials called solar absorbers.[10,11] Solar-driven technologies offer environmentally friendly[12] and cost-efficient[13] alternatives for desalination.

Solar-driven interfacial steam generation (SISG) represents an efficient approach to generating steam by converting sunlight into heat. Unlike bulk-based water heating methods, where photothermal materials are dispersed inside the bulk water and volumetrically heat the medium,[14] SISG systems are based on interface heating (localized heating), thereby preventing significant heat losses.[13,15] SISG systems are often used in remote areas with limited access to fresh water.[16–18] Recently, various studies have focused on photothermal materials, such as upcycled waste poly(ethylene terephthalate) and biomass-derived carbonaceous materials, within solar-driven interfacial steam generation (SISG) systems.[19–21] Although these systems offer advantages, such as operating independently and being environmentally friendly, challenges like the reduced efficiency of hydrophilic evaporators impede their commercial viability. As the surface of high-wetting structures is flooded with a thick layer of water, it leads to significant heat losses and decreased efficiency.[22] Janus

---

[a] *Faculty of Engineering and Natural Sciences (FENS), Sabanci University, Orhanli, 34956, Tuzla, Istanbul, Turkey. E-mail: kosara@sabanciuniv.edu, a.sadaghiani@sabanciuniv.edu*
[b] *Sabanci University Nanotechnology and Application Center (SUNUM), Sabanci University, Orhanli, 34956, Tuzla, Istanbul, Turkey*
[c] *Sabanci University Integrated Manufacturing Technologies Research and Application Center & Composite Technologies Center of Excellence, Manufacturing Technologies, Istanbul, Turkey*
[d] *Department of Mechanical Engineering, School of Engineering, University of Birmingham, Birmingham, B15 2TT, UK*
[e] *Center of Excellence for Functional Surfaces and Interfaces for Nano-Diagnostics (EFSUN), Sabanci University, Orhanli, 34956, Tuzla, Istanbul, Turkey*

† Electronic supplementary information (ESI) available. See DOI: **https://doi.org/10.1039/d4lf00082j**

‡ These authors contributed equally.

membranes, characterized by structures with asymmetric wettability, represent potential solutions to address these issues, offering a promising method for SISG by incorporating the merits of each layer.[23–25] The top hydrophobic layer is utilized for efficient solar light trapping, and the bottom hydrophilic layer is used for the water supply. In such a system, the hydrophobic layer repels water while the hydrophilic layer is immersed in water. Here, the salt could merely accumulate on the surface of the hydrophilic layer and dissolve back into the bulk water because of the continuous water pumping. This approach also may address salt accumulation, which poses another critical challenge in SISG systems. Salt accumulation limits improved water transport to the evaporator and degrades the optical properties of solar absorption.[26,27]

Several studies have recently investigated the SISG performance in Janus membranes. For example, Xiao *et al.*[28] proposed a superhydrophobic/superhydrophilic fabric composite for interfacial water evaporation within the oil-in-water emulsion. They prepared a superhydrophobic MXene-based fabric using the emulsion dip-coating method and a polydopamine-modified elastic fabric as the hydrophilic layer of the Janus membrane, which was incorporated using interfacial hydrogen bonding. This composite achieved a high energy conversion efficiency of 93.3% alongside a consistent water yield. Qin *et al.*[29] presented a novel Janus membrane made of ultralong hydroxyapatite nanowires (HNs) and glass fibers as the hydrophobic evaporator incorporated with nickel oxide (NiO) and air-laid paper as the hydrophilic water-supplying section. Their study used NiO as a p-type semiconductor photothermal material. In another study, Han *et al.*[30] introduced Janus cellulose nanofibril/$Ti_3C_2T_x$ MXene aerogels. The system's hydrophilic section provided water transportation due to the high capillary action, while the hydrophobic section was responsible for the light trapping and heat localization. The microchannels inside the evaporator also facilitated transportation of the vapor molecules to the outside of the system. Moreover, Li *et al.*[31] created a Janus fibrous membrane by combining hydrophobic MXene/poly(dimethylsiloxane) coatings with a hydrophilic polylactic acid/TiO_2 nanofluids porous fibrous membrane. When exposed to light, the MXene/PDMS coatings functioned as a photothermal layer, producing localized heat at the water–vapor interface. Meanwhile, the hydrophilic fibrous membrane served as a salt-rejection barrier induced by TiO_2 nanofluids, facilitating seawater transport to the surface through its microporous channels. The results indicated that, under 1 sun irradiation in direct contact mode, the Janus porous fibrous membrane exhibited a consistent solar-thermal conversion efficiency of 60%, a freshwater yield of 1 kg m^{-2} h^{-1}. In another study, Lv *et al.*[32] engineered a Janus membrane featuring a dual-functional evaporator by subtly modifying polydopamine (PDA) and β-FeOOH on the electrospun polyacrylonitrile surface. This membrane exhibits simultaneous capabilities for source water purification and efficient steam generation. The resultant Janus membrane demonstrates a notable evaporation rate of 1.74 kg m^{-2} h^{-1} under one sun irradiation and exhibits impressive phenol removal efficiency, with a removal rate in the condensed water of approximately 96.2%, surpassing that of simple solar interfacial evaporation by 4.9 times (19.6%).

Carbon-based materials, including carbon nanotubes (CNT),[33,34] carbonized plants,[35,36] and reduced graphene oxide (rGO),[37,38] exhibit considerable potential for light absorption across a wide spectrum and demonstrate significant photothermal conversion efficiency. These materials are highly desirable for integration into SISG systems and Janus membranes. For instance, Xu *et al.*[39] proposed a Janus membrane comprised of polyacrylonitrile (PAN) films as the hydrophilic layer and electrospun poly(methyl methacrylate) (PMMA)/carbon black (CB) as the hydrophobic layer with high efficiency (72%) and stable water output. In another study, Zhao *et al.*[40] introduced a Janus membrane composed of copper (Cu) and copper oxide/carbon aerogel, demonstrating an 88% energy conversion efficiency and 1.32 kg m^{-2} h^{-1} evaporation rate under one sun illumination. The membrane exhibits favorable characteristics, including efficient light absorption, low thermal conductivity, and high thermal diffusivity. Additionally, it demonstrates effective decontamination capabilities in sewage treatment, addressing various contaminants such as organic dyes, heavy metal ions, and pathogenic microorganisms, including bacteria, viruses, and parasites. Xu *et al.*[41] achieved a water distillation rate of 1.62 kg m^{-2} h^{-1} and an impressive photothermal conversion efficiency of 91.3% through the application of a coating comprising Ag nanoparticles and carbonated organosilica onto melamine foam. They utilized polydimethylsiloxane as a binder in this process to improve the interface adhesion and hydrophobicity of membrane. Their proposed membrane is also effective in removal of heavy metals and decontamination of dyes. In another study, Tong *et al.*[42] fabricated a Janus membrane using polysulfone hollow fiber membrane (PSF HFM) characterized by capillary force-driven water transport and three-dimensional (3D) evaporation capabilities, incorporating multi-walled carbon nanotubes (MWCNTs) as photothermal agents. The resulting 3D PSF HFMs demonstrated a high light absorption efficiency of 93.7% under simulated solar irradiation and an evaporation rate of 1.6 kg m^{-2} h^{-1} when tested with simulated seawater.

Although carbon-based materials offer numerous advantages, their usual fabrication process involves many chemical materials and incurs high costs.[43] This contrasts with the environmental benefits of the applications for which these materials are intended. This issue has prompted using environmentally friendly carbon-based materials like upcycled graphene nanoplatelets (GNP)[44] and the incorporation of recycled materials, such as carbonized photothermal materials derived from waste coffee grounds[45] or waste polyester[46] in this field.

In this study, upcycled GNP derived from the pyrolysis of waste tires is utilized as a photothermal material, and its effects on the photothermal properties of a Janus membrane are evaluated. The studies conducted to date have resulted in significant advancements and high efficiencies. However, the predominant focus of these studies has been on enhancing the properties of the materials. Concurrently, the structural parameters of the layer, which notably influence its performance, have been largely disregarded. Comprehending influential geometric parameters and examining their effects can optimize performance without requiring intricate processes, utilizing straightforward, cost-effective, and environmentally friendly materials and methodologies. Therefore, this study aims to concentrate on the parametric investigation of the Janus membrane and its impact on the ultimate performance. Accordingly, this study systematically investigates the performance of Janus membranes, determining the effect of the physical properties of the membrane and their synergistic impact on evaporation rate, photothermal activity, water purification quality, and salt resistance. Given the existing gaps in solar-driven water evaporation in Janus membranes, this study aims to theoretically and experimentally investigate the effect of thickness through a parametric study. Along with these aims, a bilayer structure included an electrospun polyacrylonitrile (PAN) nanofibrous coupled with poly(methyl methacrylate) (PMMA)/ graphene nanoplatelets (GNP) as the hydrophobic layer to fabricate a Janus nanofibrous membrane. Owing to the microporosity in the PMMA/GNP nanofibrous section, the structure provides efficient light trapping together with pathways for escaping vapor molecules after evaporation. The PAN nanofibrous membrane also provides water transportation to the surface owing to the capillary effect inside the pore structure.

Materials and methods

Fabrication methods

A Yflow Electrospinning 2.1.S-300 setup was used to fabricate a highly porous fibrous membrane. A PAN or PMMA polymer solution with a specific concentration was separately prepared based on the average molecular weight of the polymers for electrospinning. Furthermore, the preparation of the PMMA/GNP solution started with adding the 0.5% weight percentage of GNP to DMF and sonicating for 30 minutes. In the next step, PMMA was added to the solution and stirred for 24 hours at room temperature to obtain a homogeneous solution. PMMA/GNP nanofibers were initially fabricated, and then PAN nanofibers were spun on top of the PMMA layers to create hybrid systems. Sample fabrication details are demonstrated in Table 1. The thickness of each layer was adjusted by varying the electrospinning time. Increasing the electrospinning time causes the volume of the applied solution and spun fiber to increase, increasing the thickness while the surface area of the samples remains constant. Fabricated samples with their final obtained thicknesses are listed in Table 2. Their schematic and images of the sample are shown in Fig. 1.

Table 1 Details of electrospinning parameters (*D*: electrospinning distance; *V*: applied voltage during electrospinning; FR: feed rate of solution during electrospinning)

Polymer	Polymer concentration (wt%)	*D* (cm)	FR (μl min^{-1})	*V* (kV) Needle	*V* (kV) Collector
PMMA	10	28	30	10	−5
PAN	8	25	20	15	−5

Characterization

Surface topography and morphology were investigated using a drop shape analyzer, an optical microscope, and a Leo Supra 35VP field emission scanning electron microscope (SEM). The thicknesses of the layers were measured by Mitutoyo-Absolute thickness measurement (with 0.001 mm accuracy). The vibrational modes and chemical structures of the electrodes were investigated using the Nicolet IS10 FT-IR Spectrometer. Elemental X-ray diffraction (XRD) measurements were carried out by using a Bruker D2 PHASER Desktop with a CuK$_\alpha$ radiation source. A Thermogravimetric Analyzer (TGA) (Mettler Toledo TR – Model TGA/DSC3/up to 1000 °C) was used to evaluate the samples' thermal decomposition behavior. UV-visible spectrophotometer (Agilent Cary – model 5000) was utilized to determine Janus membranes' optical properties.

Experimental study

The prepared samples were placed on a polystyrene (PS) foam (with three holes filled with hygroscopic cotton), and the whole system was floated on a cylindrical container filled with distilled water. Subsequently, the container was placed on an electronic balance (ISOLAB – with 0.001 gr accuracy) under a solar simulator (ABET technologies). The mass change of the system was then monitored over time to determine the evaporation rate of the Janus membranes. A FLIR-IR thermal camera was used to characterise the photothermal activity of the samples in the dry states under one sun of illumination. The samples were exposed to the simulated sunlight while monitoring the photothermal activity with the thermography camera. Fig. 2a shows the experimental setup.

Numerical analysis

Transient numerical analyses were performed to investigate the effect of structural properties of Janus membranes on evaporation rate and liquid transportation. COMSOL Multiphysics was used to solve the conservation equations.[47,48] The governing equations include the conservation of mass, momentum, and energy at the liquid and gas phases.[49] The vapor transport through the gas phase is considered in the gas phase.

$$\frac{\partial \rho}{\partial t} + \nabla\cdot\left(\rho \vec{u}\right) = 0 \tag{1}$$

$$\frac{\partial\left(\rho \vec{u}\right)}{\partial t} + \nabla\cdot\left(\rho \vec{u}\,\vec{u}\right) = -\nabla p + \nabla\cdot\tau + \rho \vec{g} \tag{2}$$

$$\frac{\partial T}{\partial t} + \vec{u}\cdot\nabla T = \alpha + \Phi - \vec{u}\cdot\nabla C_{\mathrm{v}} + \nabla\cdot\left(D_{\text{w-air}}\nabla C_{\mathrm{v}}\right) \tag{3}$$

Table 2 The details of the fabricated samples

Sample no.	Sample details	Thickness of hydrophobic layer ($L_{PMMA/GNP}$) Thickness of hydrophilic layer (L_{PAN})
#1	Hydrophobic layer: PMMA	0.025 mm
	Hydrophilic layer: PAN	0.250 mm
#2	Hydrophobic layer: PMMA/GNP	0.025 mm
	Hydrophilic layer: PAN	0.250 mm
#3	Hydrophobic layer: PMMA/GNP	0.210 mm
	Hydrophilic layer: PAN	0.250 mm
#4	Hydrophobic layer: PMMA/GNP	0.240 mm
	Hydrophilic layer: PAN	0.150 mm
#5	Hydrophobic layer: PMMA/GNP	0.210 mm
	Hydrophilic layer: PAN	0.150 mm
#6	Hydrophobic layer: PMMA/GNP	0.120 mm
	Hydrophilic layer: PAN	0.150 mm
#7	Hydrophobic layer: PMMA/GNP	0.080 mm
	Hydrophilic layer: PAN	0.150 mm
#8	Hydrophobic layer: PMMA/GNP	0.120 mm
	Hydrophilic layer: PAN	0.066 mm
#9	Hydrophobic layer: PMMA/GNP	0.120 mm
	Hydrophilic layer: PAN	0.250 mm

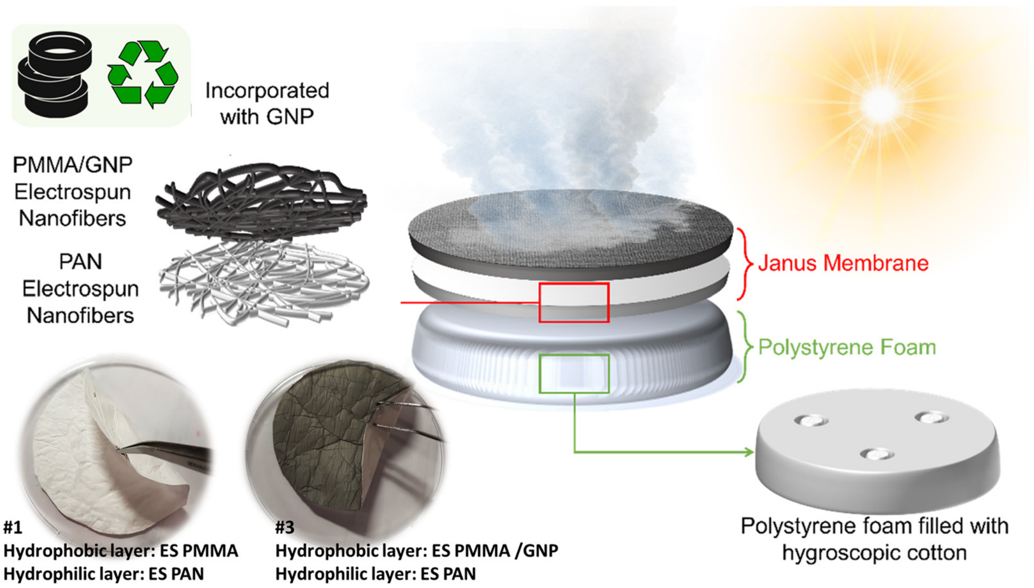

Fig. 1 Schematics and images of the prepared PAN–PMMA/GNP Janus membrane.

$$\frac{\partial C_w}{\partial t} = -\vec{u}\cdot\nabla C_w + D_i\nabla^2 C_w \qquad (4)$$

Here, ρ, u, g, p, μ, T, C_v, and C_w are the density of the fluid, velocity vector, gravitational acceleration, pressure field, viscosity, temperature, vapour concentration, and water concentration, respectively. Here, $D_{w\text{-air}}$ and D_w are the temperature-dependent diffusivity coefficients of vapor in the air and water.[50,51] Moreover, α is the thermal diffusivity of the fluid, and Φ is the viscous dissipation term. A weakly compressible approach is applied to the model to simulate natural convection in the gas and liquid domains. Regarding the small magnitude of the velocity vector and relatively small dimensions of the geometry, the flow is considered laminar in both the porous media and gas domains (Fig. 2b shows the schematic of the numerical domain).

Results and discussion

The morphology and uniformity of fabricated structures were examined through an optical microscope and SEM analysis. As can be seen in Fig. 3, a homogenous fibrous morphology with sufficient uniformity is achieved. The Image J software measured the average fiber diameter, conducting fifty

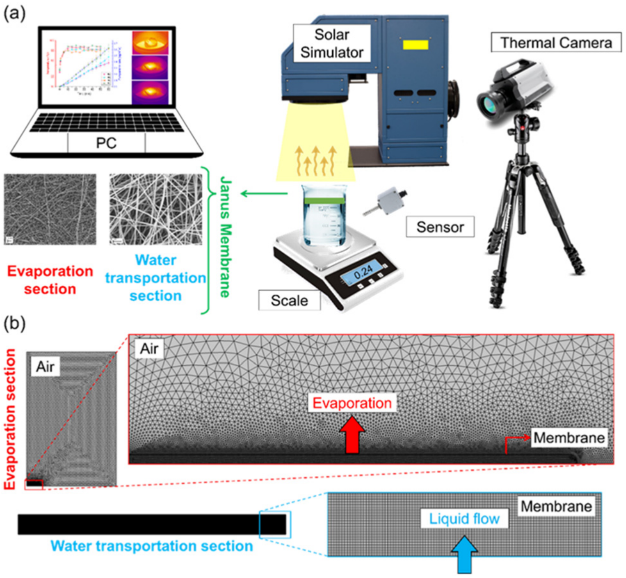

Fig. 2 (a) Schematic of the experimental setup, (b) schematic of the numerical domains. Experimental setup consisting of scale, thermal camera, solar simulator, and test section. Schematic of numerical study shows domains for evaporation and water transportation sections.

measurements for each sample. The resulting average fiber diameter of PAN, PMMA, and PMMA/GNP membranes was 250 nm, 685.5 nm, and 440.2 nm, respectively. The results show that adding the GNP concentration leads to a reduction in fiber diameter. This improvement correlates with changes in charge density induced by GNP. The increased solution conductivity improves electrospinning, yielding bead-free, uniform, and thinner fibers. This enhancement arises from increased elongation force attributable to the heightened charge density within the Taylor cone and jet.[52–54] On the other hand, incorporating a GNP concentration exceeding 0.5 resulted in instability during the electrospinning process, leading to a non-uniform layer. In fact, high conductivities lead to unsteadiness during the process, leading to a dramatic bending instability and a broad diameter distribution.[55] Therefore, a GNP concentration of 0.5% was chosen at this threshold during electrospinning.

The interaction between the GNP and the polymer (PMMA) represents another crucial factor influencing the characteristics of the resultant nanocomposite material.[56–58] Fig. 4. presents the results of FTIR analysis for GNP, pure PMMA, and PMMA/GNP nanocomposite fibrous layers. The primary absorption peaks of PMMA include 2995 cm^{-1} ($O{-}CH_3$, C–H stretching), 2947 cm^{-1} ($C{-}CH_3$, C–H stretching), 1724 cm^{-1} ($C{=}O$ stretching), 1435 cm^{-1} ($O{-}CH_3$ bending), 1389 cm^{-1} ($C{-}CH_3$ bending), 1238 cm^{-1} (C–C–O stretching), 1190 cm^{-1} (C–O–C bending), 1141 cm^{-1} (CH_2 bending), and 753 cm^{-1} ($C{=}O$ bending).[59] Distinctive features of GNPs include intense bands at 1753, 2868, 2934, and 3434 cm^{-1} corresponding to the stretching vibration of $C{=}O$ carboxylic acid, symmetric and asymmetric stretching of CH_2 groups, and stretching vibration of free –OH on the edges of graphene nanoplatelets.[60] In PMMA/GNP nanofibrous layers, similar peaks to pure PMMA are observed, except for the disappearance of the peak at 1093 cm^{-1}, typically associated with the stretching vibration of the ester C–O group. This disappearance, coupled with slight shifts in other characteristic peaks shown in Fig. 4, suggests that the addition of GNP leads to interactions with the PMMA. These interactions could impact the stretching vibrations of the ester C–O groups, causing changes in the FTIR spectrum.

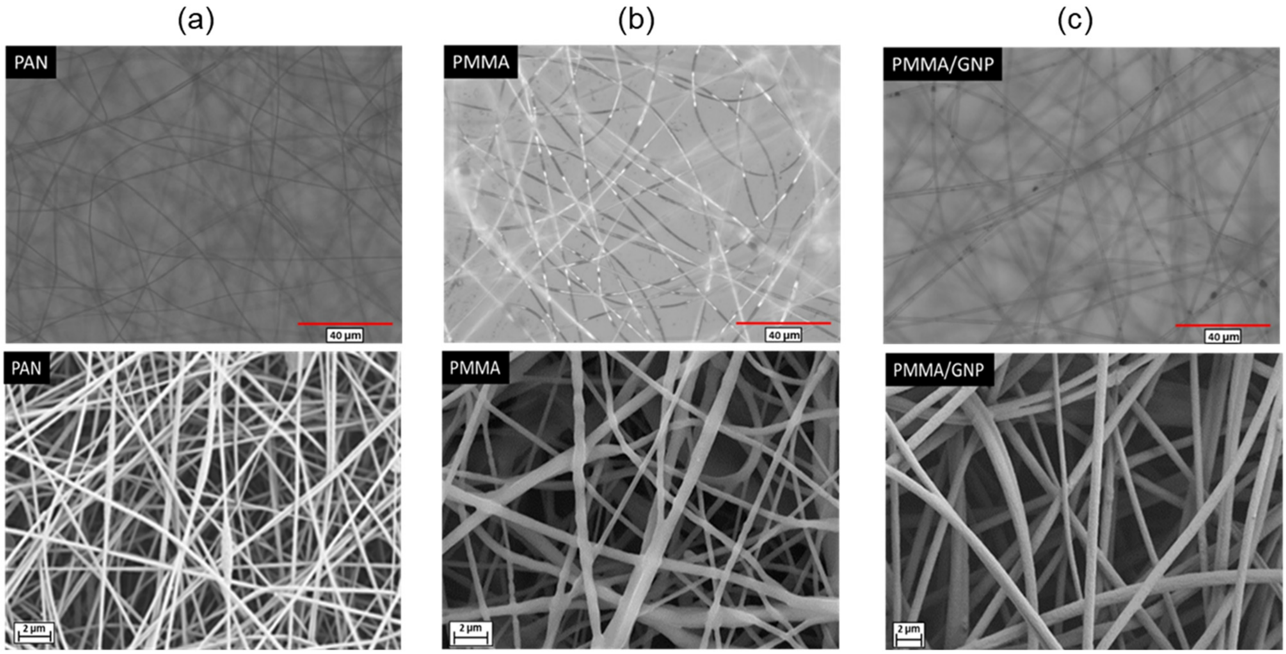

Fig. 3 Optical microscope (left) and SEM (right) images: (a) PAN nanofibers, (b) PMMA nanofibers, (c) PMMA/GNP nanofibers.

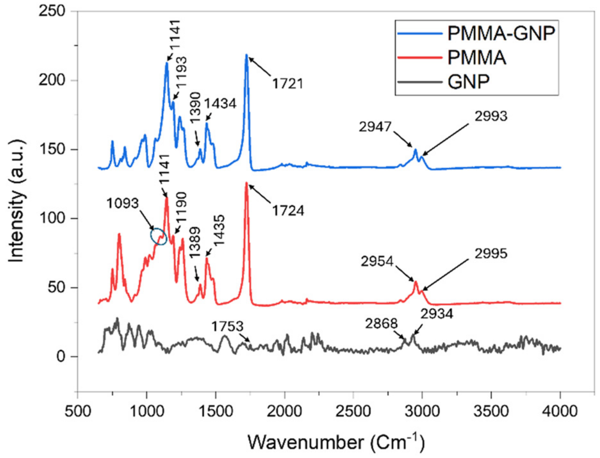

Fig. 4 FTIR spectra: pure PMMA and PMMA/GNP nanocomposites.

The static contact angles of PAN, PMMA, and PMMA/GNP electrospun membrane show that the PAN (5.4°) membrane has a hydrophilic structure, and the PMMA-based mat has hydrophobic membranes. PAN polymer chemical structure represented nucleophile –CN substitution on its surface. Therefore, PAN has a high polarity, which causes water attraction.[59] On the other hand, the PMMA chemical structure includes both hydrophobic $-CH_3$ groups and –COOR hydrophilic groups. The contact angle measurement of the PMMA electrospun membrane suggests that in the electrospinning process, most of the hydrophilic groups (–COOR) rotate underneath the surface inside the fiber; meanwhile, the hydrophobic groups ($-CH_3$) move onto the surface of the fibers.[61] With the addition of 0.5 wt% of GNP to the PMMA nanofibers, the contact angle increased to 140.8° for PMMA/GNP0.5%, thereby enhancing the hydrophobic properties of the PMMA nanofibrous layer. The contact angle images, and further characterization results (XPS, XRD and TGA) are provided in ESI† S1.

Photothermal activities and evaporation performances

This study presents a parametric investigation on a PAN–PMMA/GNP Janus membrane (Fig. 1) consisting of electrospun nanofibers forming a microporous membrane. Leveraging the advantages of nanostructures and the hydrophilic property of PAN nanofibers, this membrane enables a facilitated water pathway, functioning as a water-supplying agent in the Janus system and provides water from the bulk system to the hydrophobic evaporator.[62–64] The PAN membrane also prevents heat loss to the bulk water due to its intrinsic low thermal conductivity.[65] PAN nanofibers were spun on a PMMA/GNP nanofibrous membrane, allowing a Janus membrane with hydrophilic/hydrophobic properties. The present GNP within the PMMA/GNP evaporator works as a photothermal material capable of absorbing sunlight across a spectrum ranging from ultraviolet (UV) to near-infrared (NIR).

The PS foam was used to insulate the Janus membrane from the bulk water, facilitating the establishment and floating of interfacial water evaporation. Fig. 5a and b shows the PS foam's critical role in the membrane's transient temperature in the presence and absence of the PS foam. While the average membrane temperature reduces to 24 °C in the absence of the PS foam, the presence of PS foam acts as an insulator layer and maintains the membrane temperature as high as 60 °C. The use of the PS foam avoids unnecessary water loss from the evaporator to the surrounding bulk water. Several studies used such approaches to increase the efficiency of solar-driven water steam generation systems.[66–68] Three holes were also included on the PS foam and filled with hygroscopic cotton for water supply from the bulk water to the water-supplying PAN membrane.

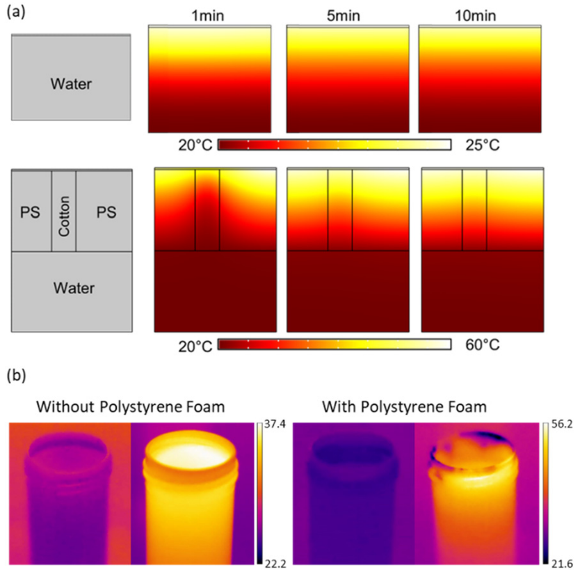

Fig. 5 The effect of the absence (top) and presence (bottom) of the PS foam on (a) transient temperature change for an initial membrane temperature of 100 °C (numerical analysis) and (b) experimental observations.

Fig. 6a and b shows the membrane surface temperature and transient weight change of the system, which were used to characterize the performance of the Janus membranes.[44,53] The evaporation performance of the tested samples was characterized using pure water under one sun of illumination.[69,70] ESI† S2 provides information regarding the stability of Janus membranes when being in contact with pure water. As seen, the evaporation rate of sample #1 (w/o carbon content) is higher than that of the blank test (pure water for w/o the presence of 3D structure). The presence of porous structure, the low thermal conductivity of 3D nanofibrous structure, and the presence of hydrophobic nanofibers at the interface are the main reasons that enhance the evaporation process. In sample #1, owing to the capillary effect, the water molecules are transported inside the microporous medium of the PAN nanofibrous membrane. However, the high hydrophobicity of the PMMA membrane does not allow the diffusion of water molecules inside this structure. According to Fig. 6c, the UV-vis spectroscopy demonstrates the capability of the Janus membranes to

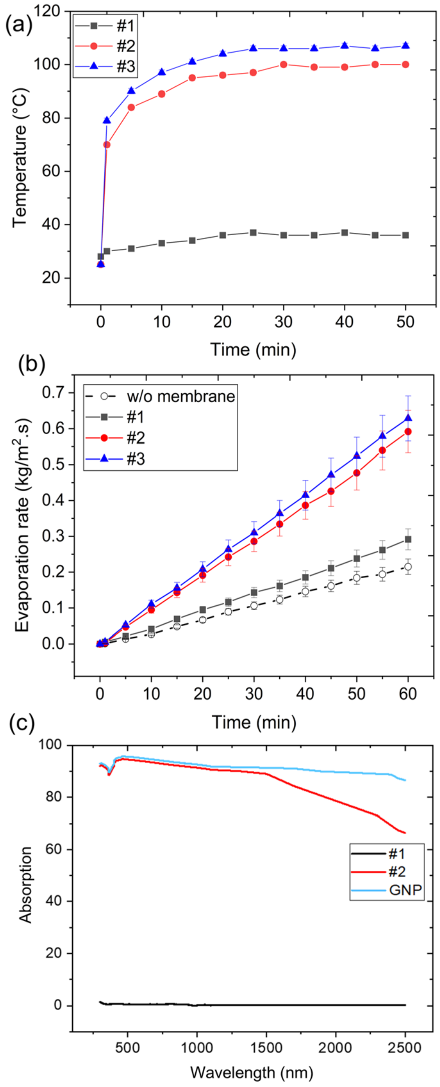

Fig. 6 (a) Dry surface temperature of the Janus membranes, (b) the evaporation rate under one sun of illumination, and (c) UV-visible absorption spectrum of the Janus membranes.

absorb solar irradiation. While sample #1 shows an insignificant value in the range of 300–800 nm spectra, there is a substantial increase in absorbance in sample #2, attributed to the presence of GNP.

Since both PMMA/GNP and PAN are porous structures, two scenarios for evaporation exist for the superimposed 3D structure (Fig. 7a). i) Evaporation of water molecules from the PAN nanofibrous membrane, where there is no contact between PAN and PMMA nanofibers. The evaporation occurs due to the break of hydrogen bonds between water molecules and the escape of these molecules in either water clusters or single molecules.[71] ii) Water Evaporation from the hydrophobic/hydrophilic nanofibers interface, as many water molecules evaporate from the hydrophobic surface. The increased thickness of the water film on the hydrophilic layer decelerates the evaporation rate as the crowd of water molecules (as a thick water film) prevents the evaporation process. On the other hand, the contact lines between water and hydrophobic nanofibers lead to enhanced performance as the water molecules diffuse from the hydrophilic region and evaporate easily through the hydrophobic surface.[72,73]

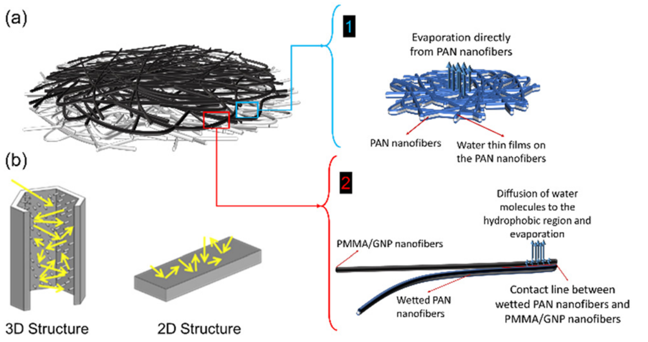

Fig. 7 (a) The effect of geometry on the light trapping in the Janus membrane, (b) a schematic of comparison between light trapping on 2D and 3D structures.

The presence of GNP in the 3D structure (*i.e.*, sample #2) significantly affects the photothermal activity in the PAN-PMMA/GNP Janus membrane. In carbon-based materials, the electrons could be excited under sunlight and generate thermal energy by electron–electron scattering following the electron relaxation.[74] The GNP increases the dry surface temperature of sample #2 compared to #1, thereby enhancing the evaporation performance in sample #2 as it increases the temperature at the air/water interface. According to Guo *et al.*, the geometry of the solar collector is also paramount for an efficient light-to-heat conversion process.[75] The microporous structure of PMMA/GNP nanofibers enables enhanced light-trapping for the Janus membrane. Fig. 7b shows the Janus membrane's mechanism for enhancing sunlight absorption. An increase in the thickness of the hydrophobic layer ($L_{\mathrm{PMMA/GNP}}$) provides more space for the light to be trapped inside the medium and converted to thermal energy. Therefore, compared to sample #2, an increase in the $L_{\mathrm{PMMA/GNP}}$ in sample #3 from 25 to 210 μm positively affects the photothermal conversion and evaporation rate.

Effect of thickness

Effect of hydrophobic membrane thickness. Fig. 8a shows the effect of evaporator layer ($L_{\mathrm{PMMA/GNP}}$) thicknesses on the temperature and evaporation rates of carbon-based 3D structures. At constant water supply layer thickness (thickness of the hydrophilic layer) (L_{PAN} = 150 μm), the temperature profiles of the tested samples indicate an enhancement trend in the photothermal activity with a decrease in the evaporator layer thickness ($L_{\mathrm{PMMA/GNP}}$ from 240 to 80 μm). Despite a slight temperature rise with the thinning of the PMMA/GNP layer, a significant enhancement in the evaporation rate could be achieved. As demonstrated, $L_{\mathrm{PMMA/GNP}}$ = 240 μm to 210, 120, and 80 μm yield an evaporation rate of 0.3863, 0.4811, 0.6155, and 0.6284 kg m^{-2} h^{-1}, respectively. This could be attributed to the decrease in molar vapor flux through the hydrophobic layer

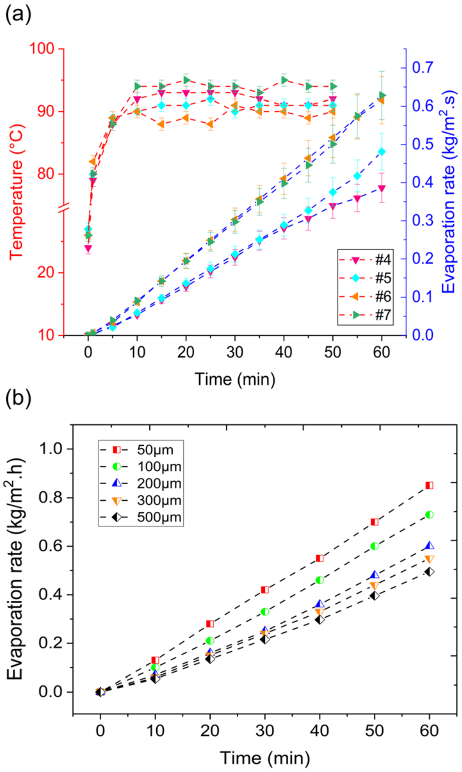

Fig. 8 (a) The dry surface temperatures and the evaporation rates by changing the thickness of the hydrophobic layer (b) obtained numerical results for the membranes with thicknesses ranging from 50 to 500 μm.

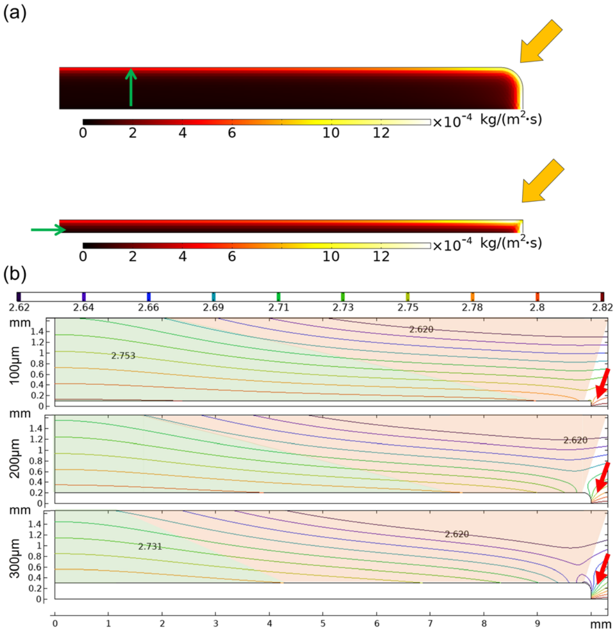

Fig. 9 Numerical results for (a) vapor concentration gradient in the evaporator section for membranes with thicknesses of 300 μm (left) and 100 μm (right), (b) the variation of vapor concentration within the membranes with thicknesses of 100, 200, and 300 μm.

due to the deterioration of membrane permeability. As included in eqn 1, the molar flux is inversely proportional to the thickness of the hydrophobic membrane:[76]

$$N \propto \frac{\langle r^{\alpha} \rangle \varepsilon}{\tau \delta} \tag{5}$$

Here, $\langle r^{\alpha} \rangle$ is the average pore size (Knudsen diffusion $\alpha = 1$), ε is the porosity, τ is the tortuosity, and δ is the thickness of the hydrophobic membrane.

Fig. 8b shows the obtained numerical evaporation rates for membranes with 5, 100, 200, 300, and 500 μm thicknesses. The transient membrane temperature is extrapolated and exerted on the model based on the average experimental results. As can be seen, the evaporation rate decreases with membrane thickness. The vapor concentration and concentration gradient during the interfacial evaporation could be a reason for such a trend.

The effect of membrane thickness on transient concentration within the membrane is shown in Fig. 9a. An increase in membrane thickness results in a larger vapor concentration gradient across the membrane (more considerable concentration resistance). Therefore, the water molecules are more concentrated at the membrane edge (shown by arrows). In addition to lower resistance to mass transfer through the membrane, a higher concentration gradient at the membrane–ambient interface enhances the evaporation rate for the membrane with 100 μm thickness (Fig. 9b). Here, the green area shows the extent of concentration from 2.7 to 2.8 (mol m^{-3}). A decrease in the green area with membrane thickness indicates evaporation rate deterioration with membrane thickness. It is worth mentioning that a high concentration gradient at the edge of the membrane with a thickness of 300 μm (red arrows) enhances the evaporation rate.

Effect of hydrophilic membrane thickness. The effect of hydrophilic membrane thickness was considered at constant $L_{\text{PMMA/GNP}}$ = 120 μm. The results indicated that bottom layer thickness does not considerably affect the photothermal activity and temperature rise (Fig. 10a), while it substantially affects the evaporation rate. Accordingly, 0.530, 0.615, and 0.635 kg m^{-2} h^{-1} evaporation rates were obtained for L_{PAN} = 66, 150, and 250 μm (samples #8, #6, and #9), respectively. Fig. 10b compares the evaporation rates of samples #8, #6, and #9. The enhancing effect of water-supplying layer thickness could be attributed to the increased water content in the PAN nanofibrous membrane. Increasing the PAN membrane's thickness enhances the water capacity, providing more water for interfacial evaporation. The pore sizes increase with the thickness of the PAN structure, meaning that the structure has higher porosity near the evaporator section.

Photothermal conversion efficiency analysis

Photothermal conversion efficiency under one sun of illumination can be calculated using the equation below:

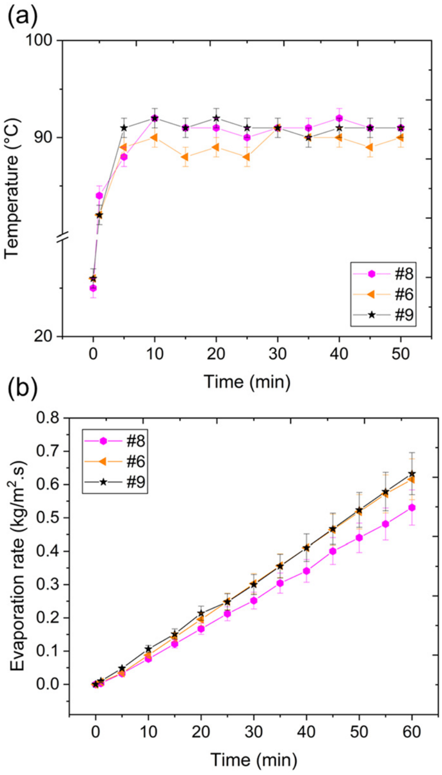

Fig. 10 (a) The dry surface temperature, and (b) the evaporation rates by changing the thickness of the hydrophilic layer.

$$\eta = \frac{m \cdot E}{Q_{\text{in}}} \tag{6}$$

where m is the evaporation rate, E is the energy consumed by evaporated water, and Q_{in} is the energy input. This parameter for sample #4, which has the thickest hydrophobic layer ($\text{LP}_{\text{MMA/GNP}}$ = 240 μm), is only 27.13%. Reducing the thickness of the hydrophobic layer to 80 μm (sample #7) resulted in a 62.75% improvement in efficiency. This means that reducing the thickness requires less material, particularly GNP, which is the most effective material in the final product, thereby reducing fabrication costs and improving the system's efficiency. On the other hand, increasing the thickness of the hydrophilic layer from 60 μm (sample #8) to 250 μm (sample #9) caused a 16.53% improvement. The maximum photothermal conversion efficiency belongs to sample #9, at 44.6%.

Sustainability analysis

This part focuses on the sustainable characteristics of the developed Janus membranes in water desalination, guided by ecological, techno-economic, and social aspects. The sustainability footprint (SF) methodology[77,78] was used to assess the impact of membranes on these aspects in the SISG system. Sustainability is analyzed using ten factors summarized in Fig. 11a. The following equation is used to assess the overall sustainable footprint (OSF) value:

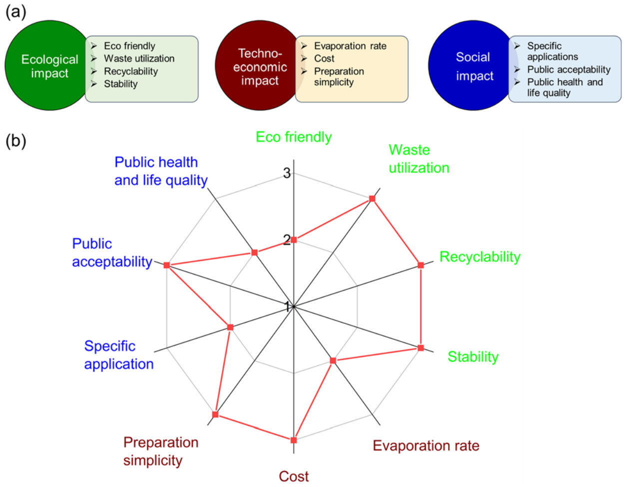

Fig. 11 (a) Sustainability factors, and (b) the sustainability analysis of developed Janus membranes.

$$\text{OSF } (\%) = \sum_{j=1}^{10} \left(\frac{i}{3}\right)_j /10 \tag{7}$$

Here, "j" represents the ten sustainability factors, and "i" represents each factor's score, which are low (i = 1, L), medium (i = 2, M), and high (i = 3, H). The greater the OSF value, the higher the sustainability of the material. Since the cost factor is a negative factor for sustainability, i = 3 means low cost, and i = 1 indicates high cost.

The rankings of several aspects are as follows: GNP, PAN, and PMMA materials have been produced on an industrial scale; therefore, the "public acceptability" of the developed membrane is ranked as 2. While the "preparation simplicity" of the electrospinning process is ranked as 3 (high), as it is used on an industrial scale, the preparation of upcycled GNP might be considered 1, and the developed bilayer membrane can be ranked 2. The "cost" associated with resources and preparation procedures for developing membranes is evaluated as 2, as the base materials are produced and used on a large scale. The "recyclability" and "waste utilization" aspects are ranked 3. While the "eco-friendly" aspect of the developed membranes is high, since they have lower advantages than bio-based membranes, they are graded as 2. According to the ranked values shown in Fig. 11b, the OSF value is 83%, among the highest values reported in the literature on membrane studies.[78–80]

Conclusion

This study proposes a systematic and parametric investigation, both theoretically and experimentally, on a Janus membrane comprising PAN nanofibers and PMMA/GNP nanofibrous membranes for solar-driven water evaporation systems. The PAN nanofibrous membrane is a suitable structure for enhanced water transport to the evaporator, allowing for a pathway for water transportation. On the other hand, the

PMMA/GNP nanofibers were hydrophobic structures hindering the diffusion of water molecules. Also, the engineered structure of the PMMA/GNP nanofibrous membrane facilitates better light trapping for the absorbed sunlight. The GNP was used as the photothermal material due to its broad light absorption range (from UV to NIR spectra), significantly increasing the photothermal activity and evaporation rate. It is worth mentioning that the GNP nanoparticles used were obtained from the pyrolysis of waste tires, which brings environmentally friendly properties and a lower carbon footprint to such systems. The following major conclusions can be drawn from the parametric study:

(i) By an increase in the thickness of the evaporator (PMMA/GNP membrane), the evaporation rate decreases as the molar vapour flux is inversely proportional to the thickness of the hydrophobic membrane.

(ii) No significant change in the photothermal activity was obtained with evaporator thickness, implying a weak correlation between the thickness of the evaporator in Janus membranes and the light-to-heat conversion.

(iii) By an increase in the thickness of the water-supplying layer (PAN nanofibrous membrane), a slight increase was observed in the evaporation rate, which could be attributed to the more available water inside the porous structure for the steam generation at the interface between PAN and PMMA/GNP membranes.

(iv) A sharp change in the wettability of the evaporator and water supply layers can be a reason for the relatively low evaporation rate in such Janus membranes. A transient change from the bottom to the top of the bilayer structure can further enhance the evaporation rate.

(v) Based on the sustainability analysis, while the ecological aspect of the developed membranes is high, the techno-economic aspect of the developed Janus membranes can be enhanced by finding the optimum GNP content for minimum cost and maximum evaporation rate.

Author contributions

JKK: investigation, formal analysis, visualization, writing – original draft, writing – review & editing; MSSB: investigation, formal analysis, writing – original draft, writing – review & editing; KD: investigation, writing – review & editing, OD: investigation, writing – review & editing, BSO: conceptualization, resources, writing – review & editing; AK: conceptualization, resources, writing – review & editing, AS: conceptualization, formal analysis, funding acquisition, investigation, project administration, writing – original draft, writing – review & editing.

Conflicts of interest

There are no conflicts to declare.

Acknowledgements

This work was supported by the Scientific and Technological Research Institution of Turkey (TUBITAK) [Grant No. 120M659]. The acknowledgments come at the end of an article after the conclusions and before the notes and references. The Faculty of Engineering and Natural Sciences (FENS), Sabanci University Nanotechnology Research and Application Center (SUNUM), and Sabanci University Integrated Manufacturing Technologies Research and Application Center & Composite Technologies Center of Excellence, Manufacturing Technologies, Istanbul, Turkey (SUIMC). The authors thank Mr. Akam Aboubakri for his support in numerical analysis.

Notes and references

1 A. Boretti and L. Rosa, *npj Clean Water*, 2019, **2**, 1–6.

2 Y. She, J. Chen, Q. Zhou, L. Wang, K. Duan, R. Wang, S. Qu, M. Xu and Y. Zhao, *Environ. Sci. Technol.*, 2024, **58**, 1119–1130.

3 A. K. Gain and Y. Wada, *Water Resour. Manag.*, 2014, **28**, 999–1012.

4 F. Tunioli, S. Khaliha, S. Mantovani, A. Bianchi, A. Kovtun, Z. Xia, M. S. S. Bafqi, B. S. Okan, T. D. Marforio and M. Calvaresi, *J. Environ. Chem. Eng.*, 2023, **11**, 109566.

5 F. Tunioli, S. Khaliha, S. Mantovani, A. Bianchi, A. Kovtun, Z. Xia, M. S. S. Bafqi, B. S. Okan, T. D. Marforio, M. Calvaresi and V. Palermo, *J. Environ. Chem. Eng.*, 2023, **11**(2), 109566.

6 H. T. El-Dessouky, H. M. Ettouney and Y. Al-Roumi, *Chem. Eng. J.*, 1999, **73**, 173–190.

7 S. A. Ravichandran, J. Hutfles and J. Pellegrino, in *Solid–Liquid Separation Technologies*, CRC Press, 2022, pp. 263–278.

8 M. Höök and X. Tang, *Energy Policy*, 2013, **52**, 797–809.

9 M. Hoel and S. Kverndokk, *Resour. Energy Econ.*, 1996, **18**, 115–136.

10 M. A. Farahat, H. E. Fath, I. I. El-Sharkawy, S. Ookawara and M. Ahmed, *Desalination*, 2021, **509**, 115078.

11 F. Nawaz, Y. Yang, S. Zhao, M. Sheng, C. Pan and W. Que, *J. Mater. Chem. A*, 2021, **9**, 16233–16254.

12 I. Ibrahim, D. H. Seo, A. M. McDonagh, H. K. Shon and L. Tijing, *Desalination*, 2021, **500**, 114853.

13 A. Anvari, A. A. Yancheshme, K. M. Kekre and A. Ronen, *J. Membr. Sci.*, 2020, **616**, 118413.

14 S. Ding, T. Zhang, M. Wu and X. Wang, *J. Membr. Sci.*, 2023, **680**, 121740.

15 H. Ghasemi, G. Ni, A. M. Marconnet, J. Loomis, S. Yerci, N. Miljkovic and G. Chen, *Nat. Commun.*, 2014, **5**, 1–7.

16 P. Tao, G. Ni, C. Song, W. Shang, J. Wu, J. Zhu, G. Chen and T. Deng, *Nat. Energy*, 2018, **3**, 1031–1041.

17 C. Chen, M. Wang, X. Chen, X. Chen, Q. Fu and H. Deng, *Chem. Eng. J.*, 2022, 137603.

18 L. Zhu, T. Ding, M. Gao, C. K. N. Peh and G. W. Ho, *Adv. Energy Mater.*, 2019, **9**, 1900250.

19 B. Chen, J. Ren, Y. Song, P. He, H. Bai, Z. Fan, R. Niu and J. Gong, *ACS Sustainable Chem. Eng.*, 2022, **10**, 16427–16439.

20 Y. Liu, H. Liu, A. Li, X. He, R. Wang, J. Yu, L. Wang and X. Qin, *ACS Sustainable Chem. Eng.*, 2023, **11**, 10845–10854.

21 X. Liu, D. D. Mishra, Y. Li, L. Gao, H. Peng, L. Zhang and C. Hu, *ACS Sustainable Chem. Eng.*, 2021, **9**, 4571–4582.

22 R. Zheng, T. Lin, W.-L. Zhao, R. Yin, H. Li, Z. Deng, W. Chen and Y.-F. Song, *Chem. Eng. J.*, 2023, 144103.

23 K. Xu, C. Wang, Z. Li, S. Wu and J. Wang, *Adv. Funct. Mater.*, 2021, **31**, 2007855.

24 S. Yu, Y. Zhang, H. Duan, Y. Liu, X. Quan, P. Tao, W. Shang, J. Wu, C. Song and T. Deng, *Sci. Rep.*, 2015, **5**, 1–10.

25 H. C. Yang, J. Hou, V. Chen and Z. K. Xu, *Angew. Chem., Int. Ed.*, 2016, **55**, 13398–13407.

26 Y. Shang, B. Li, C. Xu, R. Zhang and Y. Wang, *Sep. Purif. Technol.*, 2022, **298**, 121597.

27 A. G. Saad, S. El-Hakam, A. I. Ahmed, A. A. Ibrahim and A. Gebreil, *J. Water Process Eng.*, 2024, **58**, 104840.

28 W. Xiao, J. Yan, S. Gao, X. Huang, J. Luo, L. Wang, S. Zhang, Z. Wu, X. Lai and J. Gao, *Desalination*, 2022, **524**, 115475.

29 D.-D. Qin, Y.-J. Zhu, R.-L. Yang and Z.-C. Xiong, *Nanoscale*, 2020, **12**, 6717–6728.

30 X. Han, S. Ding, L. Fan, Y. Zhou and S. Wang, *J. Mater. Chem. A*, 2021, **9**, 18614–18622.

31 Y. Li, T. Wu, H. Shen, S. Yang, Y. Qin, Z. Zhu, L. Zheng, X. Wen, M. Xia and X. Yin, *J. Cleaner Prod.*, 2022, **347**, 131324.

32 B. Lv, S. Li, W. Wang, Y. Xu, B. Zhao, C. Song, X. Fan and Y. Liu, *J. Cleaner Prod.*, 2024, **438**, 140880.

33 M. F. Warsi, A. Ihsan, F. M. A. Alzahrani, M. H. Tariq, Z. Alrowaili, M. Al-Buriahi and M. Shahid, *Mater. Sci. Eng., B*, 2024, **301**, 117181.

34 Z. Esmaeilzadeh, B. Rezaei, A. Mousavi Shoushtari and M. R. M. Mojtahedi, *Adv. Polym. Technol.*, 2018, **37**, 185–193.

35 J. Liu, J. Yao, Y. Yuan, Q. Liu, W. Zhang, X. Zhang and J. Gu, *Adv. Sustainable Syst.*, 2020, **4**, 2000126.

36 E. Villabona-Leal, A. G. Escobar-Villanueva, E. B. Pérez-Pérez, H. Martínez-Gutiérrez and V. M. Ovando-Medina, *Int. J. Energy Res.*, 2021, **45**, 19521–19534.

37 M. Yang, T. Chu, J. Shi, J. Zhang, Y. Zhang and L. Wang, *Colloids Surf., A*, 2022, **632**, 127786.

38 R. Shu, L. Nie, Z. Zhao and X. Yang, *J. Mater. Sci. Technol.*, 2024, **175**, 115–124.

39 W. Xu, X. Hu, S. Zhuang, Y. Wang, X. Li, L. Zhou, S. Zhu and J. Zhu, *Adv. Energy Mater.*, 2018, **8**, 1702884.

40 Q. Zhao, C. Du, Y. Jia, J. Yuan, G. Song, X. Zhou, S. Sun, C. Zhou, L. Zhao and S. Yang, *Chem. Eng. J.*, 2020, **387**, 124131.

41 J. Xu, R. Cui, C. Zhou and S. Yang, *Desalination*, 2024, **573**, 117204.

42 X. Tong, C. Wei, Y. Tian, Q. Zhang, M. Wang, Z. Xu and X. Huang, *Chem. Eng. J.*, 2024, **479**, 147867.

43 D. Dey, T. Shafi, S. Chowdhury, B. K. Dubey and R. Sen, *Chemosphere*, 2024, 141164.

44 J. K. Khoei, M. S. S. Bafqi, S. Saeidiharzand, M. Mohammadilooey, M. Hezarkhani, B. S. Okan, A. Koşar and A. K. Sadaghiani, *Desalination*, 2023, 116707.

45 I. Berktas, A. N. Ghafar, P. Fontana, A. Caputcu, Y. Menceloglu and B. S. Okan, *Molecules*, 2020, **25**, 886.

46 H. Liu, L. Liu, Z. Fan, J. Liu, H. Wang, X. Wen, G. Hu, K. Liu, R. Niu and J. Gong, *Chem. Eng. J.*, 2024, 149690.

47 T. Zhang, S. Jiao, J. Zhao, G. Gao, Y. Yang and C. Guo, *Desalination*, 2022, **527**, 115576.

48 B. Chen, J. Ren, Y. Song, P. He, H. Bai, Z. Fan, R. Niu and J. Gong, *ACS Sustainable Chem. Eng.*, 2022, **10**, 16427–16439.

49 A. Sadaghiani, *Appl. Therm. Eng.*, 2021, **197**, 117359.

50 S. Saeidiharzand, A. K. Sadaghiani and A. Koşar, *Clean. Eng. Technol.*, 2022, **8**, 100495.

51 A. Aboubakri, Y. Akkus, A. K. Sadaghiani, K. Sefiane and A. Koşar, *Chem. Eng. J. Adv.*, 2022, **10**, 100255.

52 M. S. Sorayani Bafqi, R. Bagherzadeh and M. Latifi, *J. Ind. Text.*, 2017, **47**, 535–550.

53 Q. Qi, W. Wang, Y. Wang and D. Yu, *Sep. Purif. Technol.*, 2020, **239**, 116595.

54 Y. Li, H. Porwal, Z. Huang, H. Zhang, E. Bilotti and T. Peijs, *J. Nanomater.*, 2016, **2016**, 4624976.

55 M. S. Sorayani Bafqi, M. Latifi, A.-H. Sadeghi and R. Bagherzadeh, *J. Ind. Text.*, 2022, **51**, 4493S–4505S.

56 M. S. Sorayani Bafqi, R. Bagherzadeh and M. Latifi, *J. Polym. Res.*, 2015, **22**, 1–9.

57 I. Shepa, E. Mudra and J. Dusza, *Mater. Today Chem.*, 2021, **21**, 100543.

58 M. A. Scariot, B. R. Fenner, M. Beltrami, L. V. Beltrami and A. J. Zattera, *Iran. Polym. J.*, 2023, **32**, 59–69.

59 M. Muhammettursun, T. Bel, E. Kocacinar, E. Erman, F. B. Gul, A. Augousti and N. Baydogan, *J. Appl. Polym. Sci.*, 2021, **138**, 50689.

60 A. Abbasi, G. Mir Mohamad Sadeghi, I. Ghasemi and M. Shahrousvand, *Polym. Compos.*, 2018, **39**, 4020–4033.

61 X. Wang, J. Li, W. Qu and G. Chen, *J. Chromatogr. A*, 2011, **1218**, 5542–5548.

62 F. Yalcinkaya, B. Yalcinkaya, A. Pazourek, J. Mullerova, M. Stuchlik and J. Maryska, *Int. J. Polym. Sci.*, 2016, **2016**, 4671658.

63 Y. Ma, X. Cao, X. Feng, Y. Ma and H. Zou, *Polymer*, 2007, **48**, 7455–7460.

64 H.-R. Jung, D.-H. Ju, W.-J. Lee, X. Zhang and R. Kotek, *Electrochim. Acta*, 2009, **54**, 3630–3637.

65 R. Yahyapour, M. S. Sorayani Bafqi, M. Latifi and R. Bagherzadeh, *J. Mater. Sci.: Mater. Electron.*, 2022, **33**, 1783–1797.

66 S. A. Noorian, N. Hemmatinejad and J. A. Navarro, *Microporous Mesoporous Mater.*, 2020, **302**, 110199.

67 N. Sabetzadeh, H. Bahrambeygi, A. Rabbi and K. Nasouri, *Micro Nano Lett.*, 2012, **7**, 662–666.

68 L. Shi, Y. Wang, L. Zhang and P. Wang, *J. Mater. Chem. A*, 2017, **5**, 16212–16219.

69 X. Wu, Y. Wang, P. Wu, J. Zhao, Y. Lu, X. Yang and H. Xu, *Adv. Funct. Mater.*, 2021, **31**, 2102618.

70 J. Yao, Z. Zheng and G. Yang, *Nanoscale*, 2018, **10**, 2876–2886.

71 S.-L. Loo, L. Vásquez, M. Zahid, F. Costantino, A. Athanassiou and D. Fragouli, *ACS Appl. Mater. Interfaces*, 2021, **13**, 30542–30555.

72 H. Huang, L. Zhao, Q. Yu, P. Lin, J. Xu, X. Yin, S. Chen, H. Wang and L. Wang, *ACS Appl. Mater. Interfaces*, 2020, **12**, 11204–11213.

73 Y. Nagata, K. Usui and M. Bonn, *Phys. Rev. Lett.*, 2015, **115**, 236102.

74 R. Wan, C. Wang, X. Lei, G. Zhou and H. Fang, *Phys. Rev. Lett.*, 2015, **115**, 195901.

75 Y. Guo, X. Zhao, F. Zhao, Z. Jiao, X. Zhou and G. Yu, *Energy Environ. Sci.*, 2020, **13**, 2087–2095.

76 X. Li, B. Zhu and J. Zhu, *Carbon*, 2019, **146**, 320–328.

77 M. A. Aegerter, N. Leventis and M. M. Koebel, *Aerogels handbook*, Springer Science & Business Media, 2011.

78 H. Kong, Y. Chen, G. Yang, B. Liu, L. Guo, Y. Wang, X. Zhou and G. Wei, *Nanoscale Horiz.*, 2022, **7**, 112–140.

79 Y. Jiang, M. Liu, X. Zhang and Z. Su, *Desalination*, 2023, **568**, 117023.

80 G. Wei, J. Zhang, M. Usuelli, X. Zhang, B. Liu and R. Mezzenga, *Prog. Mater. Sci.*, 2022, **125**, 100915.